nature portfolio

https://doi.org/10.1038/s41563-022-01205-5

Supplementary information

3D-printed hierarchical pillar array electrodes for high-performance semi-artificial photosynthesis

In the format provided by the authors and unedited

Supplementary Information

3D-printed hierarchical pillar array electrodes for high performance semi-artificial photosynthesis

Xiaolong Chen[1], Joshua M. Lawrence[2], Laura T. Wey[2], Lukas Schertel[1], Qingshen Jing[3], Silvia Vignolini[1], Christopher J. Howe[2], Sohini Kar-Narayan[3], Jenny Z. Zhang[1*]

[1] Yusuf Hamied Department of Chemistry, University of Cambridge, Lensfield Road, Cambridge CB2 1EW, UK;

[2] Department of Biochemistry, University of Cambridge, Tennis Court Road, Cambridge, CB2 1QW, UK;

[3] Department of Materials Science and Metallurgy, University of Cambridge, 27 Charles Babbage Road, Cambridge, CB3 0FS, UK;

[*] To whom correspondence may be addressed. Email: jz366@cam.ac.uk.

Supplementary Note 1: Inverse opal and micropillar array electrodes

One of the major problems in bio-electrode design is that it has been very difficult and slow to identify bottlenecks giving rise to the lower than expected (photo)current outputs. In the case of the IO-ITO electrodes, speculations of their limitations included decrease in light penetration and loss in conductivity with increase in thickness. To determine structure-performance relationships and identify bottlenecks, the construction and characterisation of large libraries of electrodes with systematic changes to the structure are needed. This could not be easily applied to the IO-ITO structure (not without months of optimization with the introduction of each variation), and the variations to the structure were mainly limited to macro pore sizes. As such, a new way of designing and constructing electrodes are needed to progress this area.

Pillar array structures were chosen as starting points in this study since they are well-documented to exhibit distinct advantages for light harvesting. These simple structures suppress photon reflection, assist light penetration and enhance non-directional scattering of incident light compared to planar electrodes[1]. They offer a large surface-area to volume ratio, which suits catalyst integration, and have been exploited in various (bio)photoelectrochemical studies[2-4].

Pillar array structures can be produced using a range of other methods, including reactive ion etching, followed by deposition of a conductive metal coating[5], selective laser sintering[6] and imprint lithography[7]. However, to fulfil the aim of this study, we needed a technique that can simultaneously print nano, meso, micro features using materials such as ITO nanoparticles (to be comparable to the IO-ITO electrodes) in a reproducible and efficient manner. Since no present 3D-printing method could deliver this, we turned to developing a new method using aerosol jet printing.

Supplementary Note 2: Aerosol jet printing considerations for micro-pillar fabrication

During typical aerosol jet printing procedure, a non-volatile ink precursor[8,9] is aerosolized and entrained into a gas stream guided by an inert carrier gas such as N_2 (**Fig. 2a**). Another focused coaxial stream of inert sheath gas collimates the aerosol stream at the deposition head to enable high precision aerosol deposition onto a substrate[10]. The ratio of the sheath gas to carrier gas flow rate and the nozzle size can be used to tune the cross-sectional profile and diameter of the printed area independent of the ink components (equation 1 in the SI)[11]. The solvent properties of the ink precursor determine the aerosol droplet size and the rate of evaporation of the printed volume[12 13].

The ink is the aerosol precursor that typically contains nanoparticle entities dispersed in a high proportion of low-volatility solvent, with examples including silver nanoparticles dispersed in xylenes[10], or xylenes/tetralin[14], or ethylene glycol[15]. Such ink compositions were widely reported for aerosol jet printing due to the ease of fabrication and well-established working parameters such as the focusing ratio. However, the use of such inks often leads to excessive solvent content which causes line/pillar spreading, significant gravitational loss (unstable flow rate), or irregular-shaped/ill-formed pillars. The printed pillar often exhibits non-uniform "droplet-like" morphology as shown in SEM images (Fig. S1a) and results in loss of dimensional accuracy and reproducibility.

To enable focussed aerosol jet printing of micro-pillars, the ink was reformulated by tuning ratio of the volatile solvent MeOH with water at different ratios (Fig. 2c). The use of low water:MeOH ratios, gave rise to a more granular finish (Fig. S1a). The use of 1:1 water:MeOH ratios gave rise to geometrically well-controlled pillar arrays with a smooth finish (Fig. S1b). In addition to ink formulation, the aerosol printing conditions can drastically affect the aerosol droplet size printed. The gas focusing pressure ratio (GFPR, equation 2) is a new parameter identified here for enhanced control when printing micro-pillars. Although the role of the focusing ratio (FR, equation 1) in controlling line feature (horizontal printing process) is recognized, the GFPR is critical for fabricating pillar structure (vertical printing process) and for tuning pillar morphologies (Fig. 2b and Table 2). This is because the GFPR provides a way to control the diameter of carrier gas over diameter of sheath gas in the extrusion nozzle regardless of the interior gas flow speed. The gas flow rate can be easily affected by interior defects, such as clogging and leaking, which makes FR very unstable to predict the formation of micro-pillars. In contrast, GFPR is less likely to be affected by these interior defects. Therefore, the GFPR is useful in defining the ideal conditions for printing pillars.

$$\mathit{Focusing\ ratio\ (FR)} = \frac{\mathit{sheath\ gas\ flow\ rate}}{\mathit{carrier\ gas\ flow\ rate}}\text{, (equation 1)}$$

$$\mathit{Gas\ focusing\ pressure\ ratio\ (GFPR)} = \frac{\mathit{pressure\ of\ carrier\ gas}}{\mathit{pressure\ of\ sheath\ gas}}\text{, (equation 2)}$$

Supplementary Note 3: Correlation analysis

Correlation is a statistical relationship between two or more variables within a dataset. Correlation coefficients (R) measure the strength and direction of a correlation. For example, for a dataset of N samples the correlation coefficient between variables X and Y can be calculated. A strong positive correlation coefficient ($R \geq 0.7$) indicates a direct relationship between X and Y, a strong negative correlation coefficient ($R \leq -0.7$) indicates inverse relationship between X and Y, and a null correlation coefficient ($R \approx 0$) indicates no relationship between X and Y. Correlation analysis can therefore be used to predict variables (e.g. predicting the value of Y with a known value of X). Also, if one has prior information that suggests one measured variable is dependent on another, one can use correlation analysis to infer causation (e.g. an increase in the independent variable X causes an increase in the dependent variable Y). Multiple methods of correlation analysis utilising different correlation coefficients exist, and p-values can be calculated to determine if correlation coefficients are statistically significant or not. If correlation coefficients are measured for a dataset between multiple pairs of variables, these statistics can be represented in a correlation matrix.

For this study correlation coefficients were measured between the mean values of electrode properties: micro-roughness, pillar height, EASA, transmittance, reflectance, absorbance, Chl *a* loading (normalised to projection area, 0.0625 cm^2) and photocurrent density. This analysis was performed using the corrplot package in the R environment. Spearman's rank correlation coefficients, which determine how well the relationship between X and Y can be described by a monotonic function (equation 3), were calculated for each pair of variables along with p-values and displayed in a correlation matrix (Fig. 5b and Fig. S14).

$$R = 1 - \frac{6 \sum d_i^2}{n(n^2-1)} \text{ (equation 3)}$$

where R is the Spearman's rank correlation coefficient, d_i is the difference between the ranks of two variables for observation i and n is the total number of observations ($n = 12$).

The data and code used in the correlation analysis are available via the Apollo repository (DOI: 10.17863/CAM.80096) or on Github (https://github.com/JLawrence96/MicropillarArrayElectrodes).

Supplementary Note 4: Electroactive surface area characterization

We initially acquired the peak reduction/oxidation currents of the redox species of the CVs with the intention of applying the Randle Sevcik equation to calculate the EASA.:

$$i_p = 0.4463nFAC(\frac{nFvD}{RT})^{\frac{1}{2}}$$

Where i_p is the peak current; n is the number of electrons; F is the faradays constant; A is the electroactive surface area; v is the scan rate; D is the diffusion coefficient; R is the gas constant; T is the temperature.

This was based on the assumption of planar semi-infinite diffusion, which can be fulfilled when the scan rates are fast enough so that the length scales of the diffusion layer is much greater than the size of the micro-features of the electrode. Essentially, the radius of the pillars must be much greater than the diffusion layer, which can be expressed as:

$$\sqrt{Dt} \approx \delta$$

$$r \gg \delta$$

Where δ is the diffusion layer; r is the radius of micropillar.

However, after carrying the experiments, we realized that this second method did not yield sensible values because at fast scan rates (>25 mV s^{-1}), the cyclic voltammograms of 1,1'-ferrocenedimethano transitioned from reversible to quasi-reversible states. This complicated the analysis of the peak current and precluded the application of the Randles Sevcik equation in a straight forward manner.

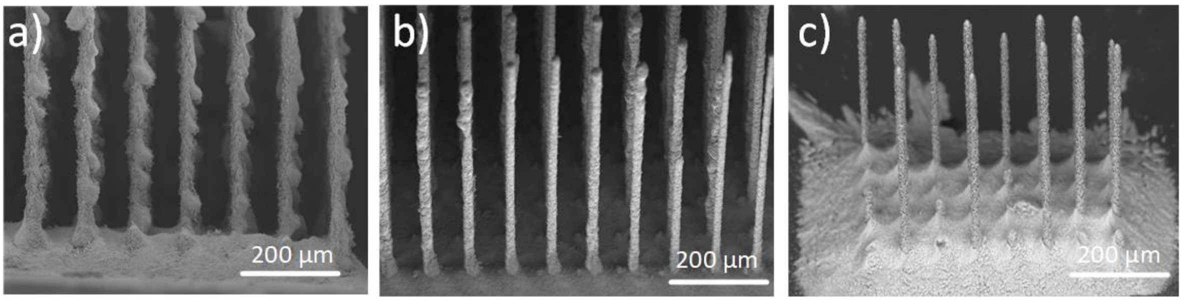

Figure S1. a) Droplet-like features on micro-pillars printed from the use of low-volatility co-solvent mixtures (methanol in water <50% v/v); b) smooth micro-pillars printed from the use of low-volatility co-solvent mixtures (methanol in water ~50% v/v); c) fragile, extremely thin micro-pillars formed from the use of high volatility co-solvent mixtures (methanol in water >75% v/v).

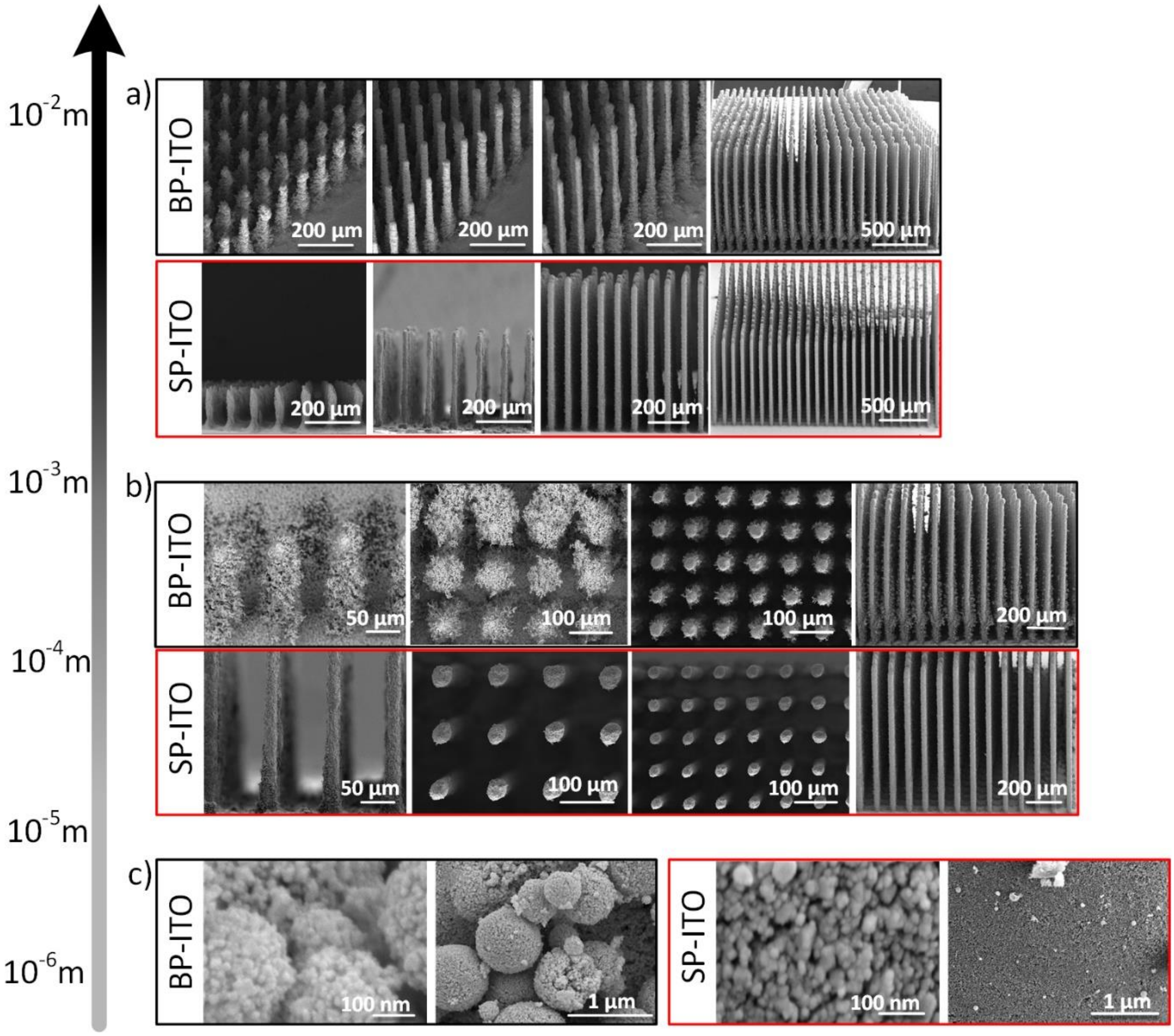

Figure S2. SEM images of BP-ITO and SP-ITO electrodes over five-orders of magnitudes in length scale.

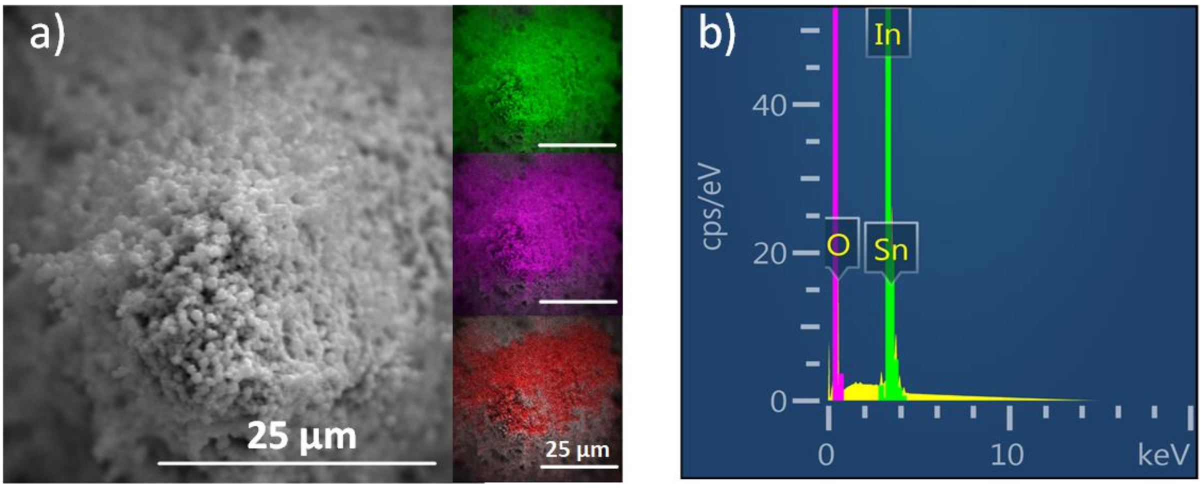

Figure S3. a) SEM image of the annealed aerosol printed electrodes; insets show the elemental distribution acquired using EDX (O in red, In in green, and Sn in purple). b) EDX elements energy spectrum showing in In green colour, Sn in yellow and O in purple.

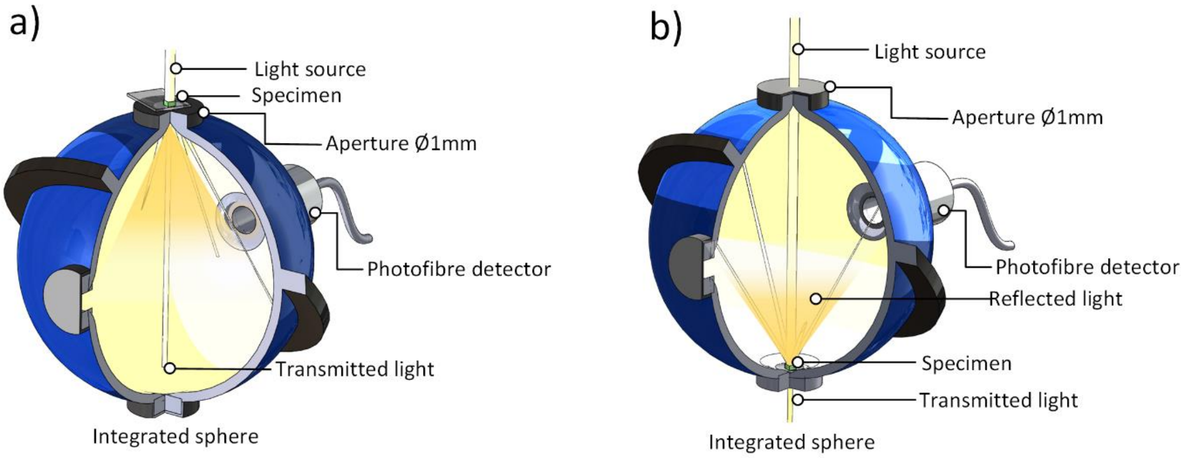

Figure S4. Schematic illustration of the integrating sphere set-up used for the light transmittance and reflectance measurements: a) configuration used for the light transmission measurements. The incident beam was transmitted through the electrode specimen and was captured by the photofibre detector on the side. b) Configuration used for the light reflection tests. The incident beam was reflected back from the sample and collected by the integrating sphere and the scattered light was led into a photofibre detector on the side. A white light source (Xenon lamp Ocean Optics HPX-2000) was used at an intensity of 0.3 mW cm^{-2} at the beam diameter was 100 µm for both measurements.

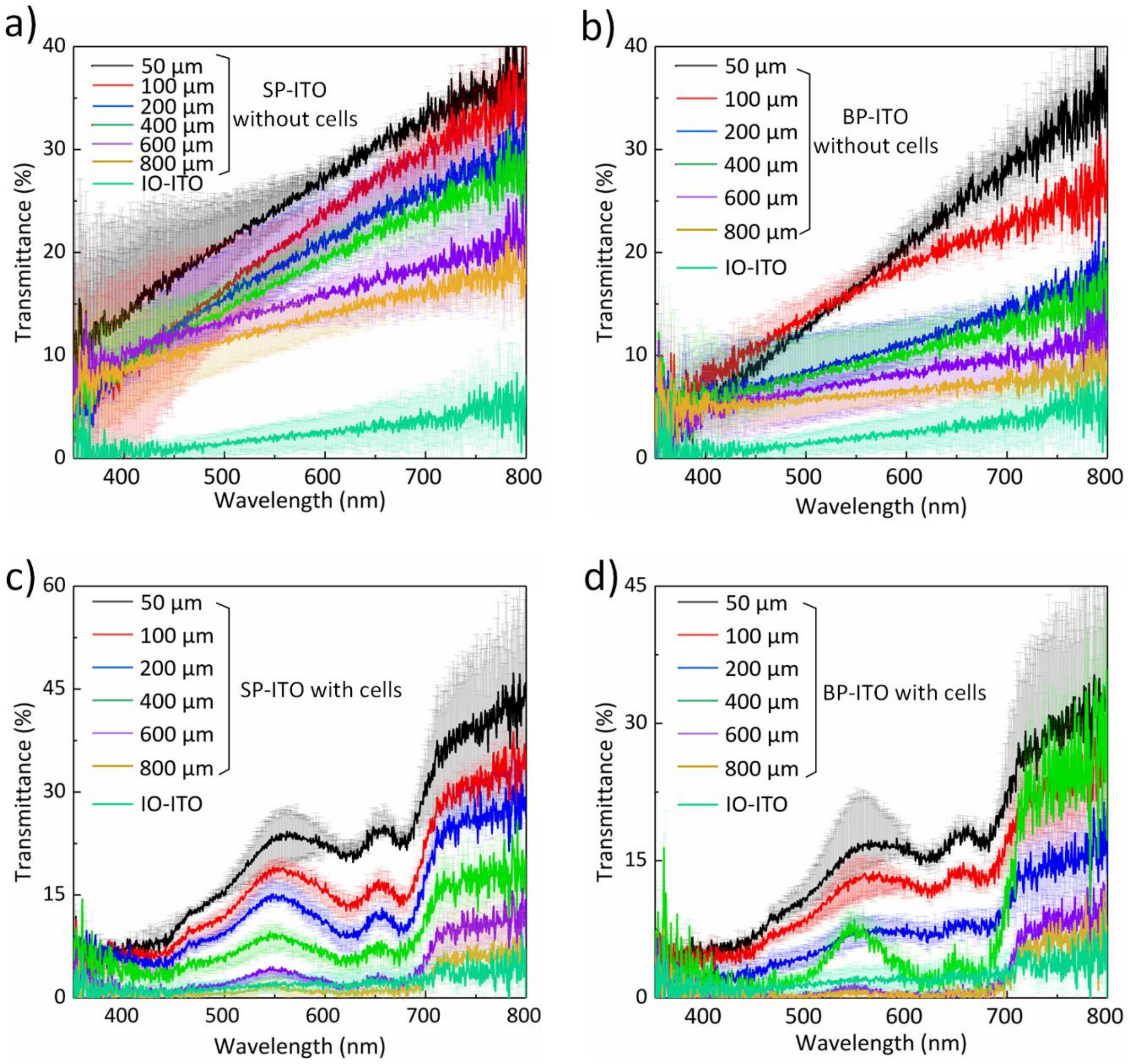

Figure S5. a) Transmittance measurement of SP-ITO and IO-ITO electrodes without loaded cells. b) Transmittance measurement of BP-ITO and IO-ITO electrodes without loaded cells. c) Transmittance measurement of SP-ITO and IO-ITO electrodes with loaded cells. d) Transmittance measurement of BP-ITO and IO-ITO electrodes with loaded cells. To load cells onto electrodes, electrodes were incubated for 12 h with *Synechocystis* before undergoing a gentle medium wash in BG11 medium and immediately used in integrating sphere measurements.

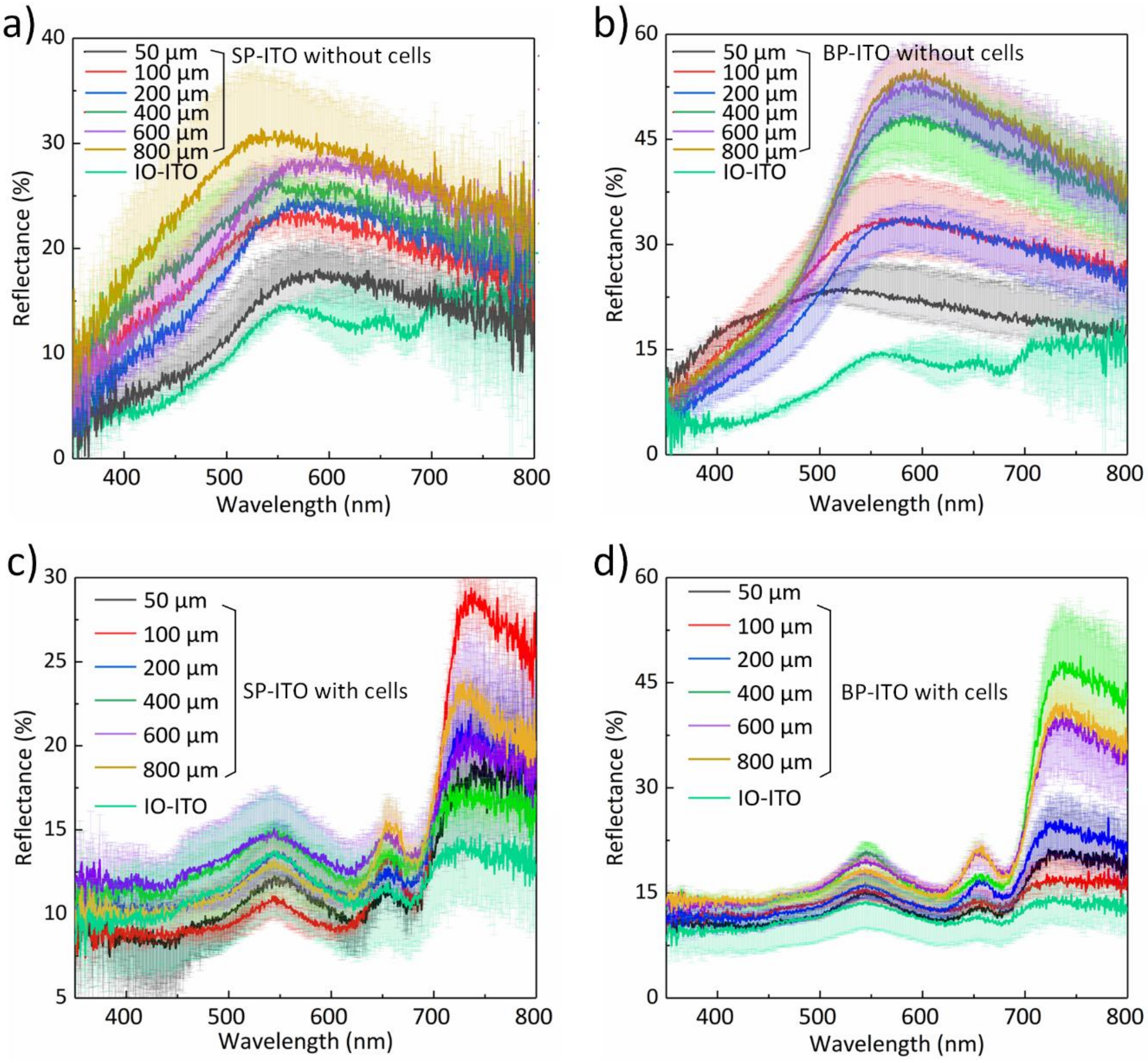

Figure S6. a) Reflectance measurement of SP-ITO and IO-ITO electrodes without loaded cells. b) Reflectance measurement of BP-ITO and IO-ITO electrodes without loaded cells. c) Reflectance measurement of SP-ITO and IO-ITO electrodes with loaded cells. d) Reflectance measurement of BP-ITO and IO-ITO electrodes with loaded cells. To load cells onto electrodes, electrodes were incubated for 12 h with *Synechocystis* before undergoing a gentle medium wash in BG11 medium and immediately used in integrating sphere measurements.

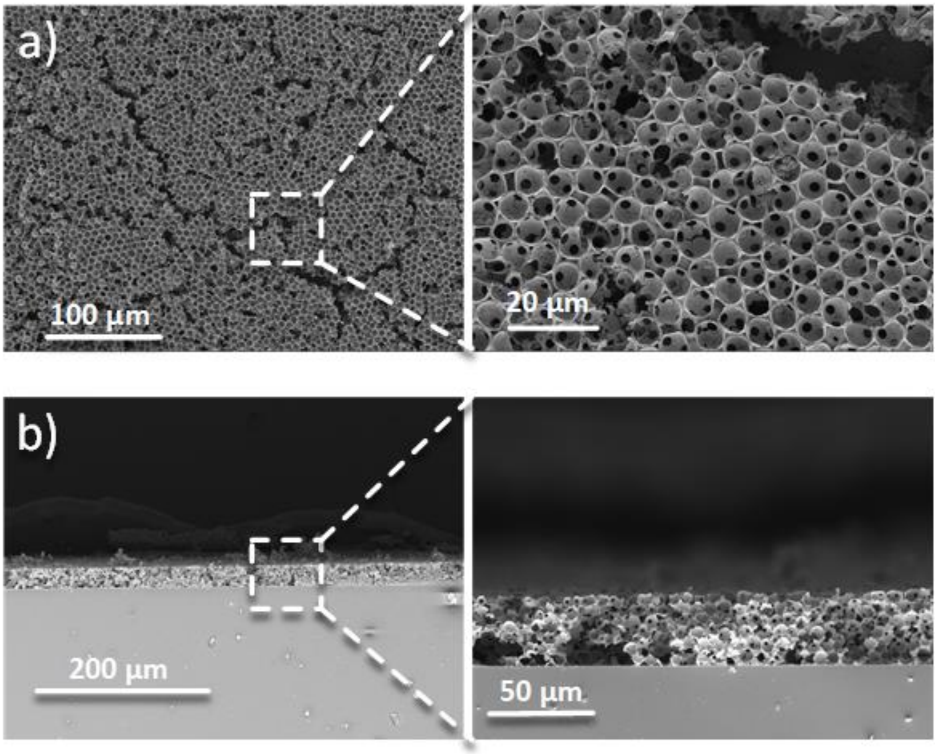

Figure S7. a) SEM images IO-ITO electrodes (top view), b) SEM images of IO-ITO electrodes (cross-section).

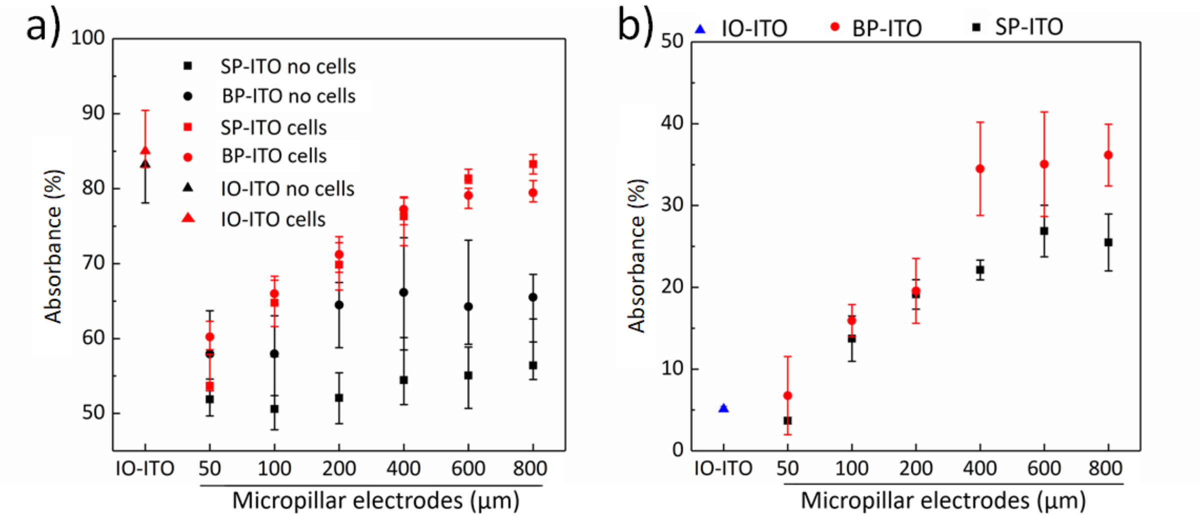

Figure S8. a) Light absorbance of the IO-ITO (height of 50 µm), SP-ITO and BP-ITO electrodes (with pillar heights 50 - 800 µm) with and without *Synechocystis* cells loaded. b) Difference in light absorbance between *Synechocystis*-loaded electrodes and bare electrodes, which is attributed to absorbance by the cyanobacterial cells on the electrodes.

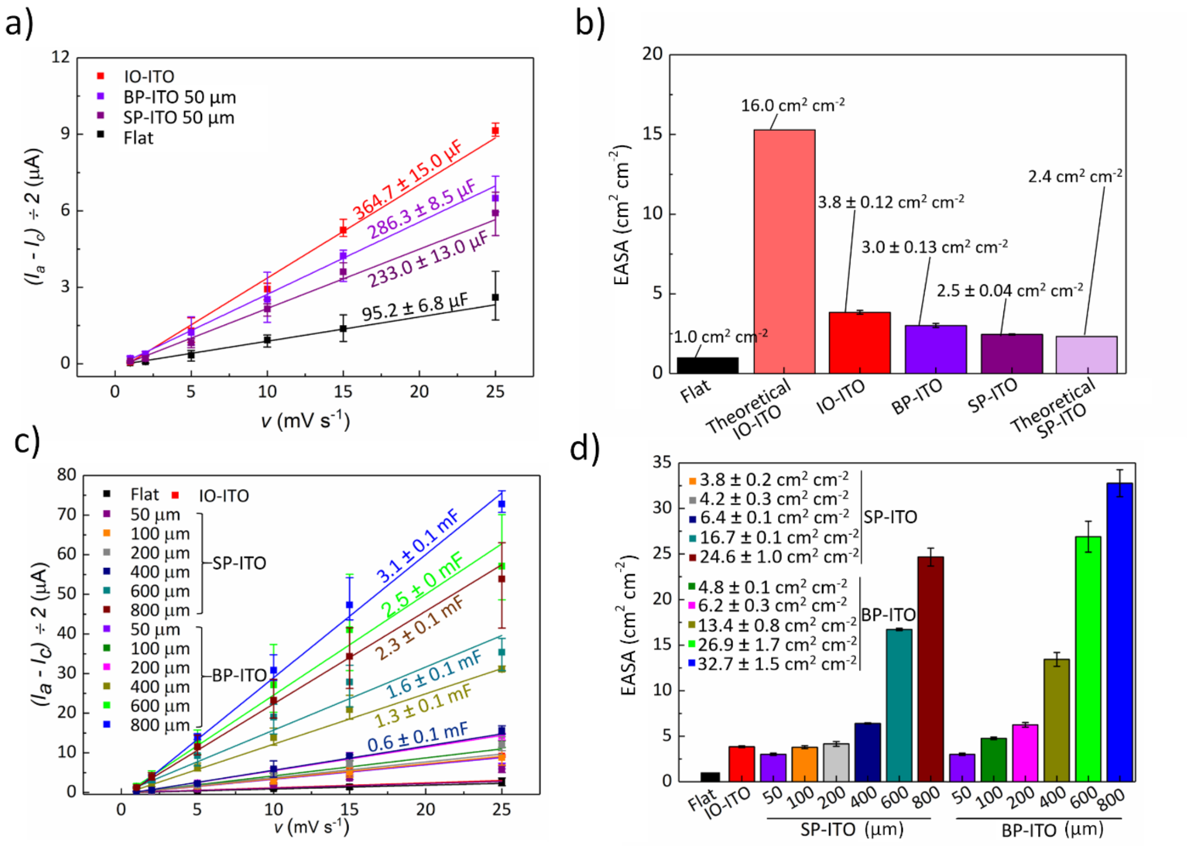

Figure S9. a) Summary of capacitance measurements used to calculate the electrochemically-active surface area (EASA) of IO-ITO electrodes (height: 50 µm), SP-ITO electrodes (height: 50 µm), BP-ITO electrodes (height: 50 µm) and aerosol sprayed flat electrodes. b) Summary of measured EASAs normalised to aerosol sprayed flat ITO electrodes compared against theoretically calculated valuables. c) Summary of capacitance measurements used to calculate the EASA of IO-ITO electrodes (thickness: 50 µm), SP-ITO electrodes (height: 50 µm up to 800 µm), BP-ITO electrodes (height: 50 µm up to 800 µm) and aerosol sprayed flat electrodes. d) Summary of EASAs normalised to aerosol sprayed flat ITO electrodes for SP-ITO electrodes (height: 50 µm up to 800 µm), BP-ITO electrodes (height: 50 µm up to 800 µm). EASA were determined by performing cyclic voltammetry at different scan rates and calculating the capacitance at 0.3 V vs. SHE.

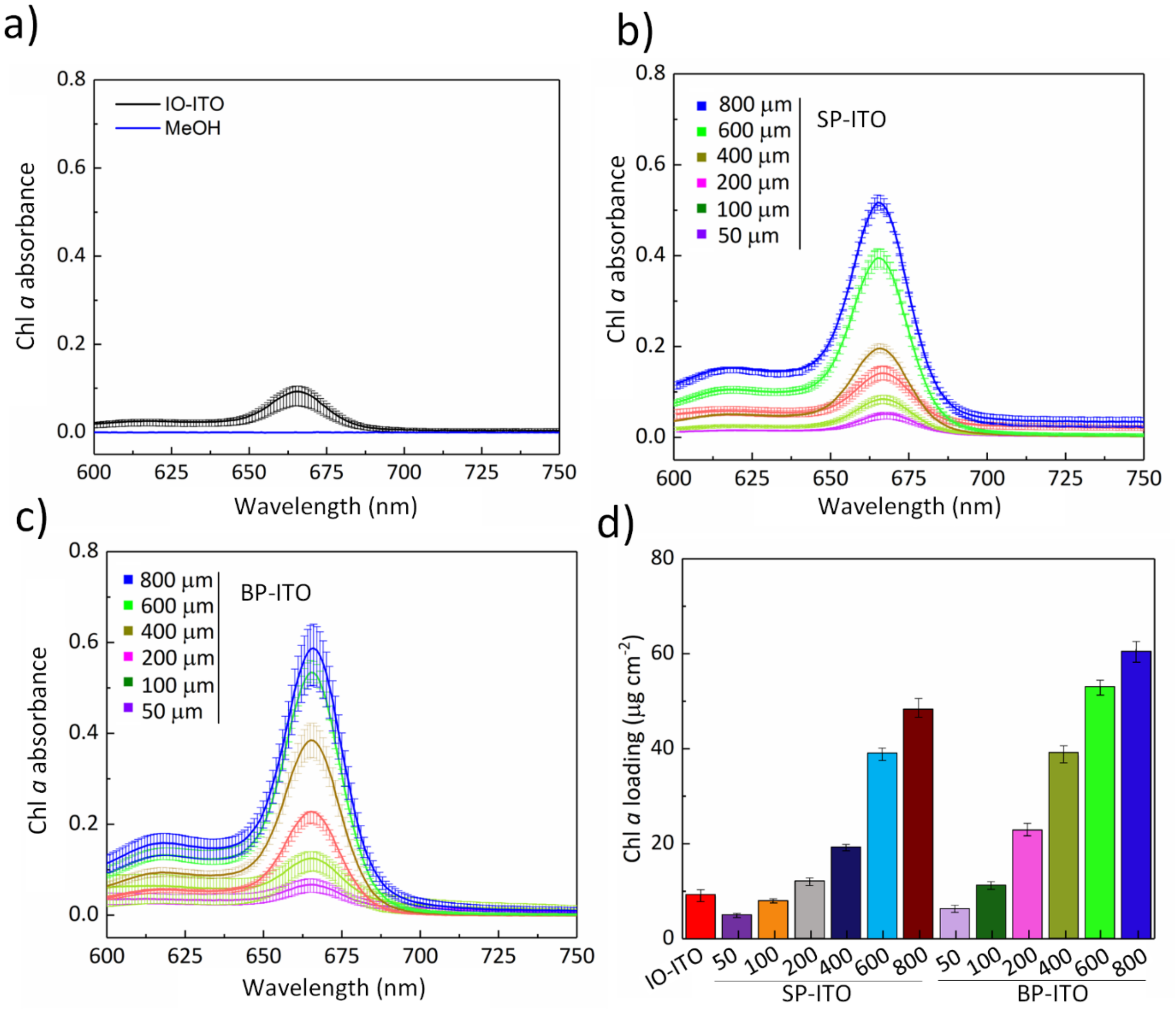

Figure S10. Total Chl *a* loading on electrodes following 12 h incubation with *Synechocystis* and a gentle wash in BG11 medium. a) Chl *a* loading on IO-ITO electrodes; b) Chl *a* loading on SP-ITO electrodes; c) Chl *a* loading on BP-ITO electrodes; d) Summary of the Chl *a* absorbance difference between wavelength of 665 nm and 750 nm.

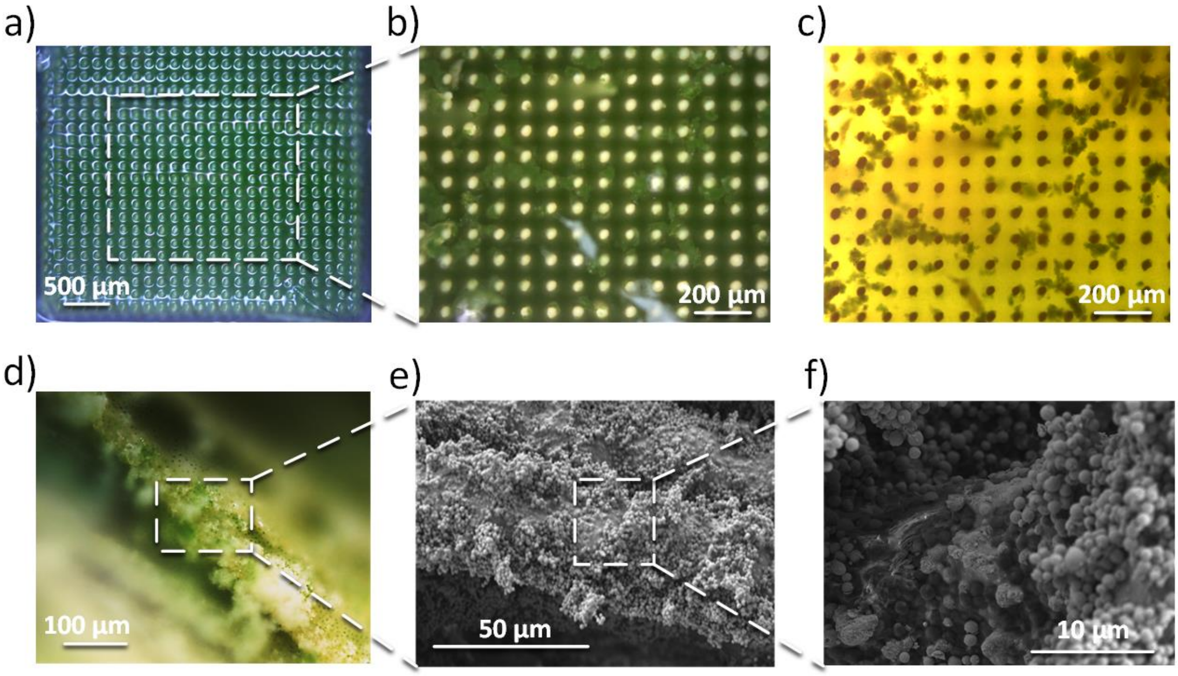

Figure S11. A representative BP-ITO electrode (600 µm in height) following 12 h incubation with *Synechocystis* and a gentle electrolyte wash. a) An optical microscope image of *Synechocystis*-loaded BP-ITO electrode immersed in BG11 media; b) an enlarged top view of the optical microscope image; and c) an enlarged bottom view of the optical microscope image. d) Optical microscope image of the *Synechocystis*-loaded BP-ITO electrode after air-drying for SEM imaging. e) SEM image of *Synechocystis*-loaded BP-ITO electrode; and f) an enlarged SEM image of *Synechocystis*-loaded BP-ITO electrode showing cells amongst the ITO micro-structures.

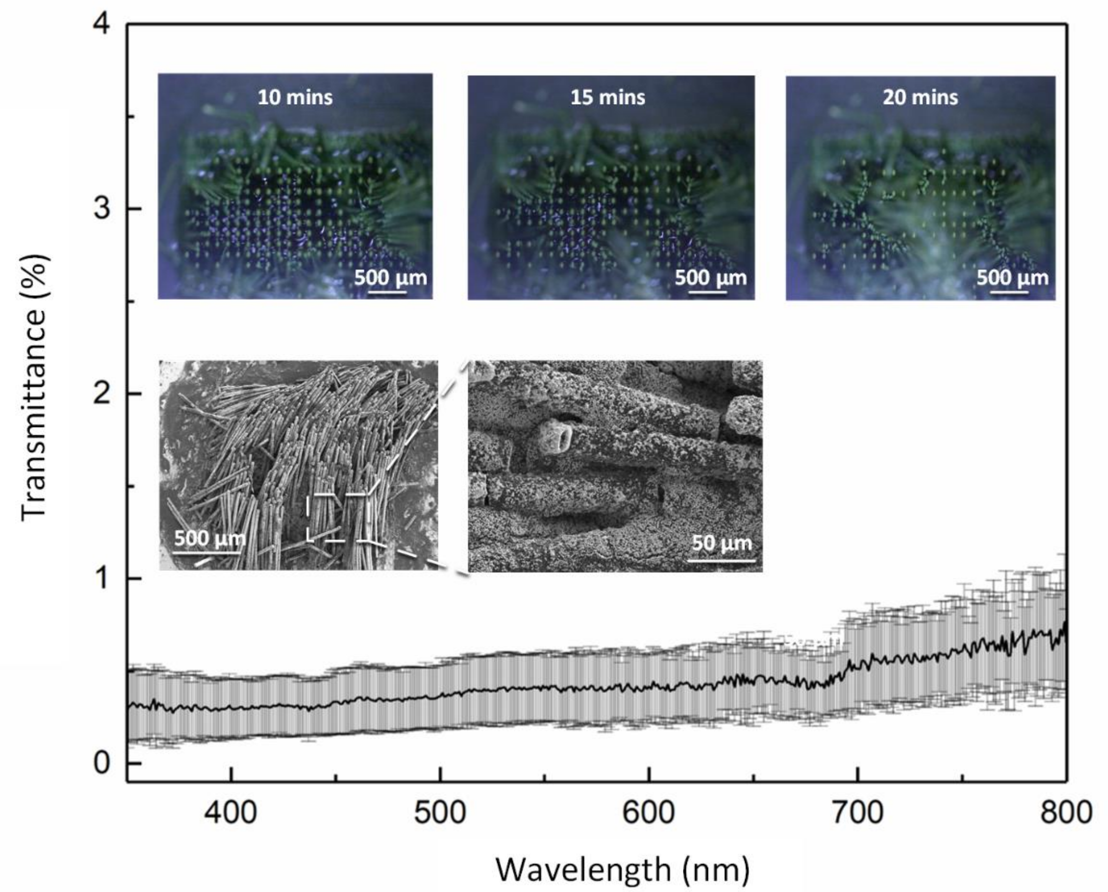

Figure S12. Transmittance measurement of a collapsed SP-ITO micropillar array electrode (height of 600 µm) loaded with cells. The collapse of SP-ITO micropillar was induced by evaporation conditions[16]. Insert: Optical microscope images show a time-lapse of the collapsing micropillar due to strong capillary forces. SEM images show a folded over micropillar electrode loaded with cells. This collapse led to a change in electrode transmittance that was two orders of magnitude lower than upright pillars.

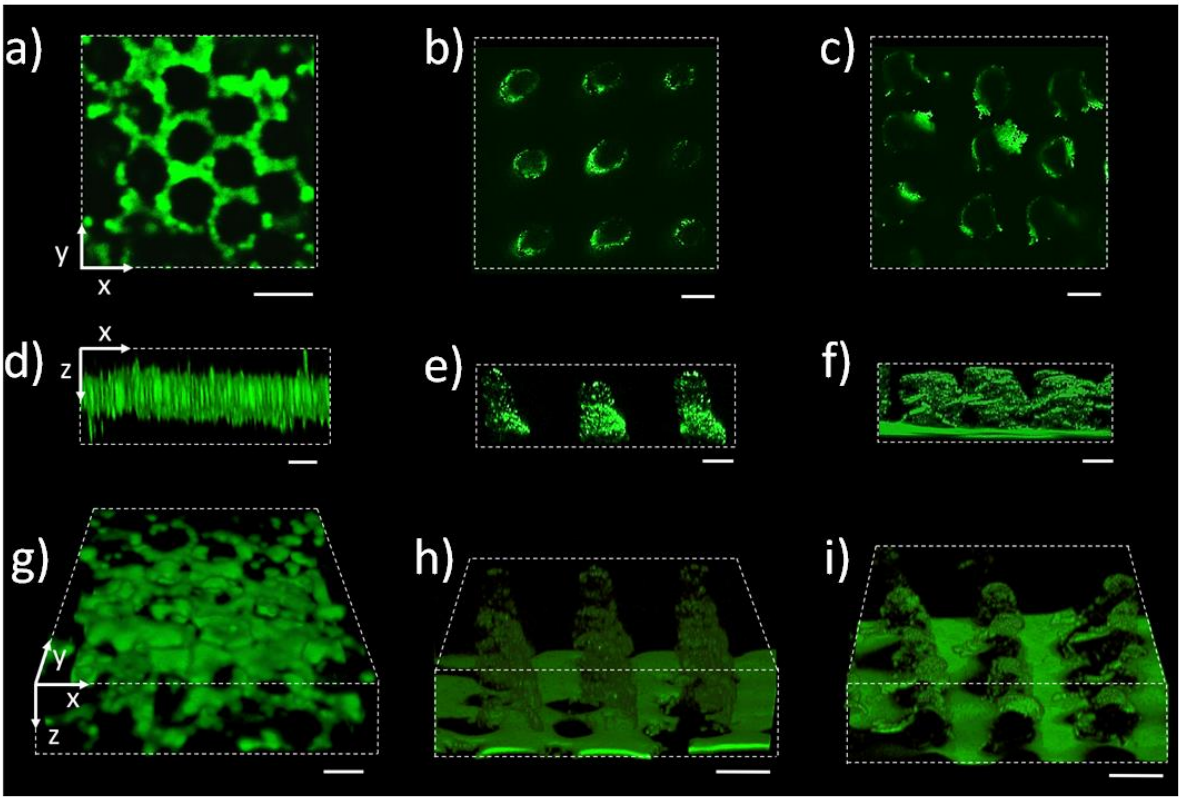

Figure S13. Confocal microscopy visualisations (Z-stacks) of cyanobacteria distribution on *Synechocystis*-loaded electrodes. Top section views of *Synechocystis*-loaded a) IO-ITO, b) SP-ITO and c) BP-ITO electrodes (all with heights of 50µm). Side views of *Synechocystis*-loaded d) IO-ITO, e) SP-ITO and f) BP-ITO electrodes. Tilted angle 30º views of *Synechocystis*-loaded g) IO-ITO, h) SP-ITO and i) BP-ITO electrodes. Excitation: λ_{ex} = 633 nm; emission: λ_{em} = 650 -750 nm. Scale bar in a) 10 µm, in b)-i) 20 µm.

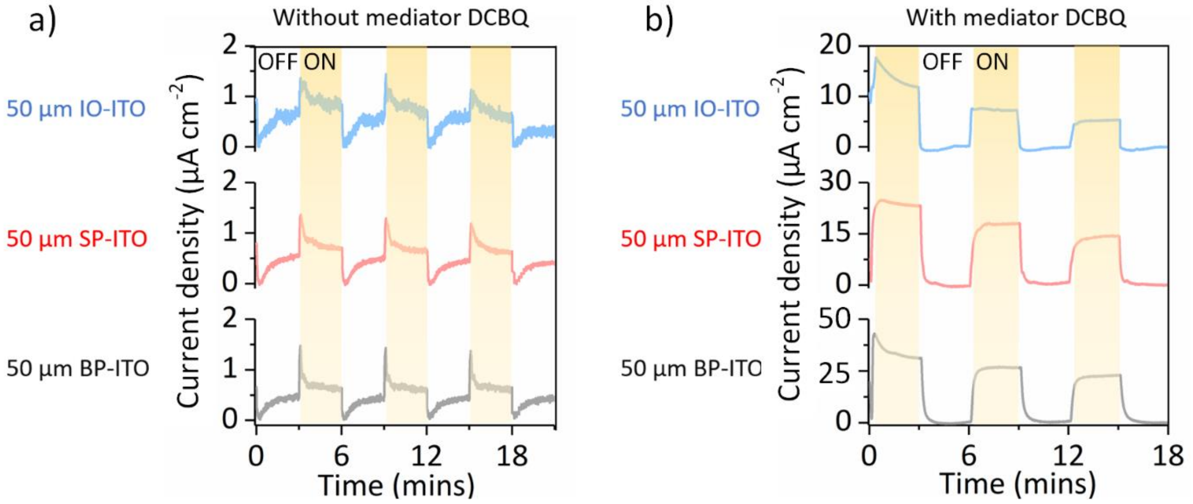

Figure S14. Representative photocurrent output of *Synechocystis*-loaded IO-ITO, SP-ITO and BP-ITO electrodes (50 µm height) in the presence and absence of the exogenous electron shuttle, DCBQ with concentration of 1 mM, Chronoamperometry experiments were performed with an applied potential of 0.3V and 0.5V vs SHE in the absence and presence of DCBQ, respectively, and in BG11 (pH 8.5) at 25 ºC. Light source used: λ_{680nm}: 1 mW cm^{-2}.

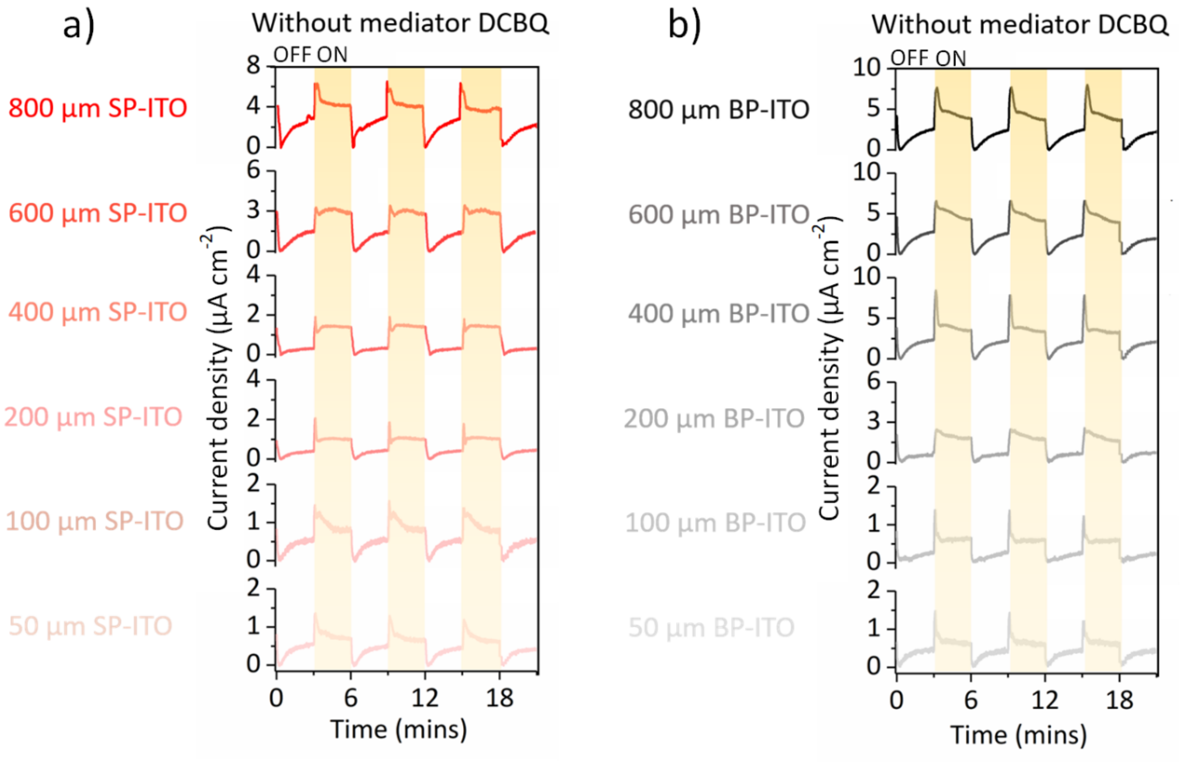

Figure S15. Representative photocurrents of *Synechocystis*-loaded SP-ITO and BP-ITO electrodes of varying pillar heights. Chronoamperometry experiments were performed with an applied potential of 0.3 V vs. SHE in BG11 (pH 8.5) at 25 ºC. Light source used: λ_{680nm}: 1 mW cm^{-2}.

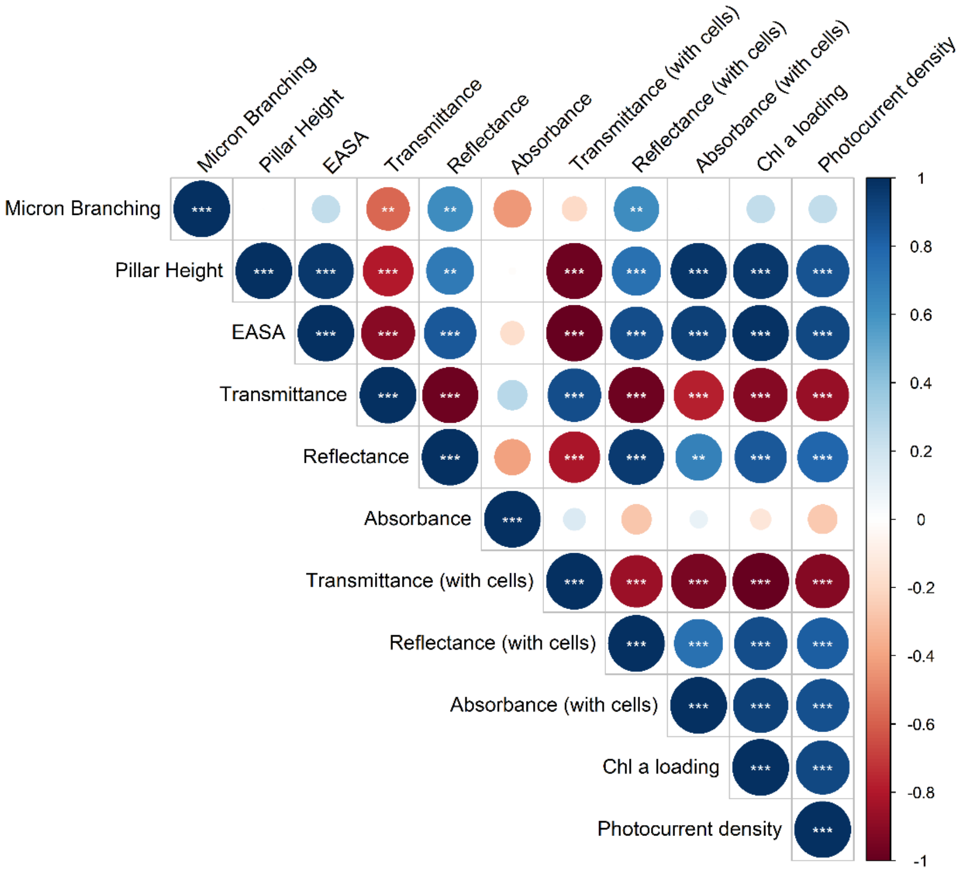

Figure S16. Spearman's rank correlation matrix of micro-pillar electrodes and their properties, including the optical properties of electrodes loaded with cells. The scale bar represents the strength and sign of the correlation coefficient (R), with blue indicating a positive and red a negative correlation coefficient. Stars indicate significance where $*$ is $p \leq 0.1$; $**$ is $p \leq 0.05$ and $***$ is $p \leq 0.01$.

Table S1 Properties of aerosol droplets printed as a result of different water/methanol solvent compositions. Droplets were aerosol jet printed within a glovebox under 25°C, using nanoparticle density 360 kg/L, N_2 pressure of 3.5 KPa, and excitation frequency of the atomizer 0.42 mA.

Water/methanol ratio	**Methanol % (v/v)**	**Surface tension of solvent mixture (σ)**[17]	**Droplet size (d_p)**
Methanol only	100.0	21.59 mN/m	N/A
1:6	86	20.2 mN/m	1.75 µm [a]
1:3	75	25.1 mN/m	1.87 µm [a]
1:1	50	28 mN/m	2.01 µm [a]
3:1	25	34 mN/m	2.10 µm [a]
6:1	14	40 mN/m	2.21 µm [a]
Water only	0	71.40 mN/m	N/A

[a] Droplet size was calculated based on equation[18].

Table S2. Aerosol printing conditions for building micro-pillar library

	BP-ITO						SP-ITO					
Height of pillar (μm)	50	100	200	400	600	800	50	100	200	400	600	800
Focusing pressure ratio	2.3 - 3						2.3 - 3					
MeOH (%V/V)	65 - 75						50 - 65					
Geometric size (cm^2)	0.0625						0.0625					
Printing time (s/pillar)	0.01 - 0.05	0.03 - 0.1	0.1 - 0.3	0.5 - 0.8	1 - 1.5	2 - 4	0.01 - 0.05	0.03 - 0.1	0.1 - 0.3	0.5 - 0.8	1 - 1.5	2 - 4
Centre-to-centre spacing (μm)	100						100					
Base thickness (μm)	< 20						< 20					

Table S3. Summary of electrode performances (λ: 685 nm, 1 mW cm^{-2}) at 25°C

BP-ITO (DET)	E_{app} *(V vs. SHE)*	J (μA cm $^{-2}$)	I (mW cm^{-2})	EQE (%)
Height 600 um	0.3	1.72 ± 0.05	1	0.31 ± 0.01
BP-ITO (MET)	E_{app} *(V vs. SHE)*	J (μA cm $^{-2}$)	I (mW cm^{-2})	EQE (%)
Height 600 um	0.5	158 ± 4.7	1	28.6 ± 0.85

References:

1 Deng, J. *et al.* Nanowire photoelectrochemistry. *Chemical reviews* **119**, 9221-9259 (2019).

2 Su, Y. *et al.* Close-packed nanowire-bacteria hybrids for efficient solar-driven CO2 fixation. *Joule* **4**, 800-811 (2020).

3 Champigneux, P. *et al.* Effect of surface nano/micro-structuring on the early formation of microbial anodes with Geobacter sulfurreducens: experimental and theoretical approaches. *Bioelectrochemistry* **121**, 191-200 (2018).

4 Zhao, Y. *et al.* From Geometry to Activity: A Quantitative Analysis of WO3/Si Micropillar Arrays for Photoelectrochemical Water Splitting. *Advanced Functional Materials* **30**, 1909157 (2020).

5 Cho, I. S. *et al.* Branched TiO2 nanorods for photoelectrochemical hydrogen production. *Nano letters* **11**, 4978-4984 (2011).

6 Zhao, C. *et al.* Three dimensional (3D) printed electrodes for interdigitated supercapacitors. *Electrochemistry Communications* **41**, 20-23 (2014).

7 Sun, P., Li, X., Shao, J. & Braun, P. V. High‐Performance Packaged 3D Lithium‐Ion Microbatteries Fabricated Using Imprint Lithography. *Advanced Materials* **33**, 2006229 (2021).

8 Martinez-Acosta, A., Tafoya, R. R., Quinones, S. A. & Secor, E. B. Modular motion control software development to support a versatile, low-cost aerosol jet platform for printed electronics. *Additive Manufacturing*, 101932 (2021).

9 Tafoya, R. R. *et al.* Real-Time Optical Process Monitoring for Structure and Property Control of Aerosol Jet Printed Functional Materials. *Advanced Materials Technologies* **5**, 2000781 (2020).

10 Mahajan, A., Frisbie, C. D. & Francis, L. F. Optimization of aerosol jet printing for high-resolution, high-aspect ratio silver lines. *ACS applied materials & interfaces* **5**, 4856-4864 (2013).

11 Kopola, P. *et al.* Aerosol jet printed grid for ITO-free inverted organic solar cells. *Solar energy materials and solar cells* **107**, 252-258 (2012).

12 Williams, B. A. *et al.* Formation of copper zinc tin sulfide thin films from colloidal nanocrystal dispersions via aerosol-jet printing and compaction. *ACS applied materials & interfaces* **7**, 11526-11535 (2015).

13 Yang, C., Zhou, E., Miyanishi, S., Hashimoto, K. & Tajima, K. Preparation of active layers in polymer solar cells by aerosol jet printing. *ACS applied materials & interfaces* **3**, 4053-4058 (2011).

14 Secor, E. B. Principles of aerosol jet printing. *Flexible and Printed Electronics* **3**, 035002 (2018).

15 Saleh, M. S., Hu, C. & Panat, R. Three-dimensional microarchitected materials and devices using nanoparticle assembly by pointwise spatial printing. *Science advances* **3**, e1601986 (2017).

16 Roman, B. & Bico, J. Elasto-capillarity: deforming an elastic structure with a liquid droplet. *Journal of Physics: Condensed Matter* **22**, 493101 (2010).

17 Santos, B., Ferreira, A. & Fonseca, I. Surface and interfacial tensions of the systems water+ n-butyl acetate+ methanol and water+ n-pentyl acetate+ methanol at 303.15 K. *Fluid Phase Equilibria* **208**, 1-21 (2003).

18 Rajan, R. & Pandit, A. B. Correlations to predict droplet size in ultrasonic atomisation. *Ultrasonics* **39**, 235-255 (2001).

End of supplementary information